A novel technique for rapid L^* calculation: Algorithm and implementation

Kyungguk Min,[1] Jacob Bortnik,[2,1] and Jeongwoo Lee[1,3]

[1]   Computing the magnetic drift invariant, L^*, rapidly and accurately has always been a challenge to magnetospheric modelers, especially given the importance of this quantity in the radiation belt community. Min et al. (2013) proposed a new method of calculating L^* using the principle of energy conservation. Continuing with the approach outlined therein, the present paper focuses on the technical details of the algorithm to outline the implementation, systematic analysis of accuracy, and verification of the speed of the new method. We also show new improvements which enable near real-time computation of L^*. The relative error is on the order of 10^{-3} when $\sim 0.1\ R_E$ grid resolution is used and the calculation speed is about 2 s per particle in the popular Tsyganenko and Sitnov 05 model (TS05). Based on the application examples, we suggest that this method could be an added resource for the radiation belt community.

1.   Introduction

[2]   Constrained by the large-scale electric and magnetic fields of the inner magnetosphere, the dynamics of energetic particles in the Earth's radiation belts are most conveniently expressed and visualized with the aid of three adiabatic invariants [e.g., *Roederer*, 1970; *Schulz and Lanzerotti*, 1974]. In the terrestrial magnetosphere, these adiabatic invariants are associated with three periodic motions: gyration around the magnetic field, bounce motion along the magnetic field line between magnetic mirror points in the Northern and Southern Hemispheres, and gradient/curvature drift across the magnetic field, leading to motion around the Earth. These adiabatic motions are well separated by their adiabatic time scales, and the adiabatic invariants are conserved as long as the external field remains quasi-static on each invariant time scale [e.g., *Cary and Brizard*, 2009].

[3]   Computation of the first two invariants requires only the local magnetic field (single point) or its magnitude along the field line (one-dimensional line) where the guiding center of the particle is located. Computation of the third invariant (L^*) is, however, computationally more demanding because the particle drift shell in the global magnetic field (and electric field in general) must be known. Because the global magnetic field is difficult to measure, if not impossible, one must rely on magnetic field models to obtain this drift shell. As *McCollough et al.* [2008] demonstrated, computation of the drift shell and L^* is evidently dependent upon the complexity of the model field used (exceeding well over 10 days to compute 1 day worth of L^* values in the Tsyganenko 02 (T02) model [*Tsyganenko*, 2002a, b], Table 5 in *McCollough et al.* [2008]). These authors also demonstrated that using a simpler model (i.e., a faster model) with 2% difference in the model field can produce as much as a 10% difference in the resulting L^*.

[4]   Several libraries and methods that compute L^* values are currently available. International Radiation Belt Environment Modeling (IRBEM) (http://sourceforge.net/projects/irbem) [*Boscher et al.*, 2012] implements the technique introduced by *Roederer* [1970], in which adjacent field lines with the same magnetic field magnitude at a mirror point and the same second invariant as the initial value are iteratively searched until the drift shell is completed. Recently developed, LANLGeoMag (M. Henderson, http://www.rbsp-ect.lanl.gov), currently providing the orbits of Van Allen Probes [*Mauk et al.*, 2012] in L^* coordinates, can compute various magnetic ephemerides including L^* in real time. LANLGeoMag numerically solves the particle's guiding center equation of motion to obtain the drift shell and can achieve an accuracy as high as nine decimal places. LANL* [*Koller et al.*, 2009; *Koller and Zaharia*, 2011; *Yu et al.*, 2012], unlike the previous two methods that are based on first principles (referred to as physics-based methods), uses a Neural Network that predicts L^* values at a given parameter set based on the statistical L^* values that were calculated at many independent parameter sets. The calculation speed of this Neural Network is on the order of a 10th of a second, and the relative error is about 3×10^{-2} ($\Delta L^* < 0.2$) at geosynchronous orbit [*Koller and Zaharia*, 2011].

[1]Center for Solar and Terrestrial Research, Department of Physics, New Jersey Institute of Technology, Newark, New Jersey, USA.
[2]Department of Atmospheric and Oceanic Sciences, University of California, Los Angeles, California, USA.
[3]School of Space Research, Kyung Hee University, Yongin, South Korea.

Corresponding author: K. Min, Center for Solar and Terrestrial Research, Department of Physics, New Jersey Institute of Technology, Newark, NJ, USA. (km224@njit.edu)

[5] Recently, *Min et al.* [2013] (referred to as Paper 1 hereafter) proposed an efficient method of computing L^* values. The method is similar to the technique introduced by *Roederer* [1970] in that it uses conserved quantities to obtain the drift trajectory. The main differences are, however, as follows: first, unlike the technique of *Roederer* [1970], the trajectory is obtained by drawing the iso-energy contour from the discrete 2-D energy space defined by constant first and second adiabatic invariants. This approach ensures that the calculated trajectory is closed if the particle's drift shell is so, regardless of the grid resolution. Second, the functional relationship between B_m and K is approximated before the L^* calculation (Sheldon and Gaffey [1993] used a polynomial expression and *Min et al.* [2013] used spline interpolation), where B_m is the magnitude of the magnetic field at a mirror point s_m and K is the modified invariant [*Roederer*, 1970]

$$K = \int_{s'_m}^{s_m} \sqrt{B_m - B(s)}\,ds. \tag{1}$$

In this expression, s'_m denotes the conjugate mirror point to s_m so that $B(s'_m) = B(s_m) \equiv B_m$, and the integration is made along the guiding field line s. Once the model coefficients are known, $B_m(K)$ or $K(B_m)$ is approximated from the functional form whenever they are needed, avoiding the repeated expensive field line tracing.

[6] In Paper 1, the functional relationship between B_m and K in every magnetic field configuration was calculated at every x-y grid point in advance. The advantage is that once tabulation of the coefficients is done, calculating iso-energy contours is very fast. As described in Paper 1, this approach is very efficient for multiple calculations of L^* values for a given magnetic field configuration but can be impractical in applications where a relatively small number of L^* values in many different field configurations need to be computed, for example, to track the orbits of satellites in L^* coordinates in real time. In this technique paper, we address and focus on the technical improvement that enables near real-time calculation while not degrading the speed of calculating many L^* values. Following a short description of underlying physics, section 2 describes the algorithm and implementation in detail, while section 3 analyzes performance. Section 5 demonstrates a simple application, and section 6 summarizes the paper.

2. Algorithm and Implementation

2.1. Formulation

[7] In a static electric and magnetic field, the dynamics of charged particles are completely described by three conserved quantities in the guiding center approximation: μ, J (or K), and W, which are linked by

$$W = qU + m\gamma c^2 = qU + mc^2 \sqrt{1 + 2\mu B_m/mc^2}, \tag{2}$$

where W is the total energy of the particle; U is the electric potential; $\mu = p_\perp^2/2mB(s)$ is the first adiabatic invariant; q and m are charge and rest mass of the particle, respectively; c is the speed of light; $\gamma = \sqrt{1 + 2\mu B(s)/mc^2 + p_\parallel^2/(mc)^2}$ is the Lorentz factor; and $p_{\parallel(\perp)}$ is the momentum parallel (perpendicular) to the magnetic field. The second adiabatic invariant

$J = \oint p_\parallel\,ds$ is related to μ and B_m through equation (2). Equation (2) can be approximated by $W - mc^2 \simeq mv_\parallel^2/2 + qU + \mu B(s) = qU + \mu B_m$ for nonrelativistic particles, which is analogous to the motion of a particle in a one-dimensional potential well defined by $qU + \mu B(s)$ [e.g., *Roederer*, 1970]. Since W remains constant while a particle drifts for the given μ and K, the trajectory is conveniently obtained from the coordinates of the iso-energy contour. Note that all the variables in equation (2) are implicitly a function of the position. In general, U can be an arbitrary function as long as the guiding approximation is valid, but in the Earth's magnetospheric environment, the electric field along the field line is usually assumed to be zero, in which case J can be replaced with a more convenient form $K\sqrt{2m\mu}$ which only depends on the field line geometry.

[8] Once the drift orbit of a particle is defined, evaluation of the magnetic flux Φ contained within the drift orbit of the particle is then obtained by integrating

$$\Phi = \oint \mathbf{A} \cdot d\mathbf{l} = \int_A \mathbf{B} \cdot d\mathbf{a}, \tag{3}$$

where $\mathbf{A}$ is the vector potential of the magnetic field $\mathbf{B}$. Note that the integration of the vector potential form is taken along the closed contour defined by the drift orbit. In other words, Φ is defined only if the drift orbit of the particle is closed. The second form of the integration is usually preferred because the magnetic field is well defined from the model. The areal integration can be easily performed over the area A on the polar cap defined by the footpoints of the guiding field lines [*Roederer*, 1970]. L^* is then the ratio of Φ_0 to Φ, where $\Phi_0 = -2\pi k_0$ and k_0 is the Earth's magnetic moment.

2.2. Functional Dependence of B_m on K: $B_m(K)$

[9] In order to evaluate equation (1) with constant μ and K at a given field line, B_m and U should be functions of those parameters. With the equipotential field line, U is only a function of 2-D spatial coordinates (in this paper, x-y coordinates with z set to zero), and B_m is a function of x-y coordinates and K (hereinafter the dependence on the spatial coordinates is implicitly assumed). In general, $K(B_m)$ given in equation (1) is neither integrable nor invertible. Indeed, the numerical evaluation of K is the most computationally expensive part of the technique of *Roederer* [1970] due to the necessity of field line tracing.

[10] To approximate the functional dependence of B_m on K (i.e., $B_m(K)$) from equation (1), *Sheldon and Gaffey* [1993] used a 10th-order polynomial approximation which results in only 3% maximum deviation, whereas Paper 1 used spline interpolation for the same purpose, resulting in 0.1% deviation at maximum (with approximately 1° pitch angle resolution). In this paper, we approximate $B_m(K)$ using linear interpolation as we found that the resulting error in L^* has the same order of magnitude. For evaluation of equation (1), only the real part is taken into account [*Northrop and Teller*, 1960; *Sheldon and Gaffey*, 1993]. The field line is integrated using a Runge-Kutta fourth-order scheme. We use fixed step size rather than adaptive step size (cf. Paper 1) to measure accuracy and calculation speed in a more consistent fashion. During the field line integration, various auxiliary parameters
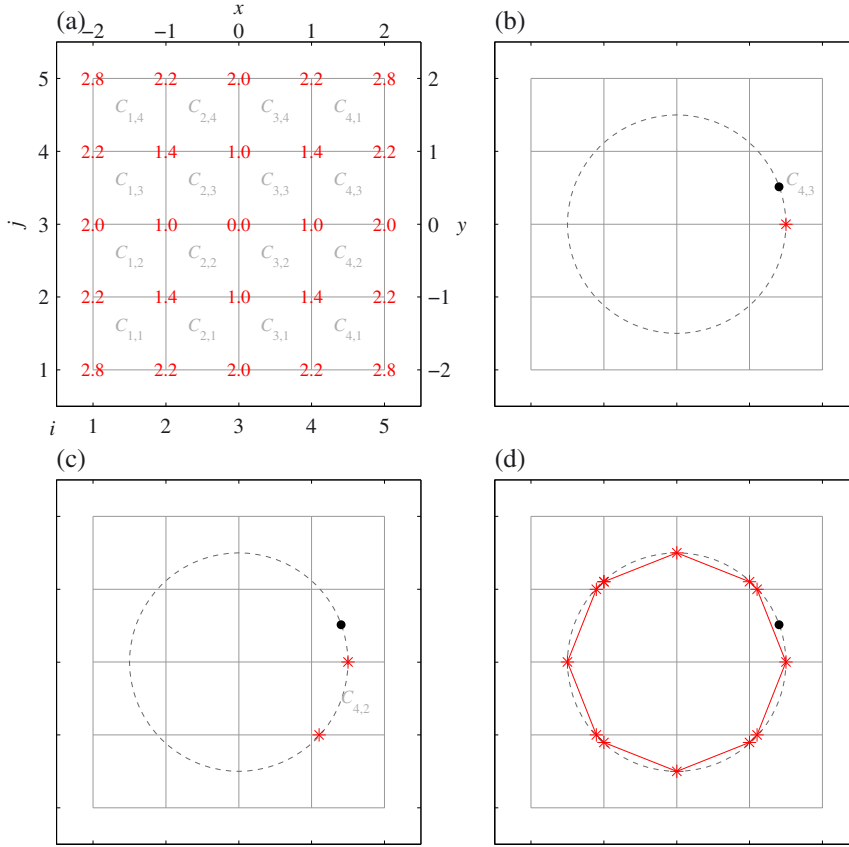
Figure 1. Schematic diagram of the tracing algorithm. (a) x-y coordinate space and index space. Index coordinates are on the bottom and left axes, and the corresponding x-y coordinates are on the top and right axes. The cells are labeled following the definition in the text. The values of our example energy at the grid nodes are labeled with red color. (b–d) A demonstration of the iteration process. The heavy dot locates the initial location of the test particle, the dashed circle is the analytic contour line, and the solid curve is the estimated contour line by the algorithm. The intersections that the contour line passes are marked with asterisk symbols.

such as loss cone angles at each field line, footpoints on the Earth's surface, and magnetic field magnitudes at the magnetic equator are also obtained.

2.3. Drift Orbit From Iso-energy Contour

[11] The basic concept follows the algorithm of *Sheldon and Gaffey* [1993]. The x-y space is discretized, and the total energy $W(x_i, y_j, \mu, K)$ in equation (2) are calculated in this grid space. Here (x, y) is used to denote the coordinate of an arbitrary point, and (x_i, y_j) is used to denote the coordinate of the grid node at (i, j)th index. Any quantities located at (x, y) are approximated by areal interpolation using the quantities at four nodes adjacent to (x, y). For the purpose of description, we define a "cell" $C_{i,j}$ as a square box that connects vertices $(i, j) - (i + 1, j) - (i + 1, j + 1) - (i, j + 1) - (i, j)$ in the index space, and Edges 1–4 as edges of the cell connecting the vertices in that order. In this definition, $C_{i,j}$ shares Edge 2 with $C_{i+1,j}$, which shares Edge 4 with $C_{i,j}$. The same analogy is applied to other edges. Figure 1a is an example of mapping between the index space and rectangular grid space. Using this general index space frees the dependence on the underlying coordinate system and thus enables modular implementation.

[12] Figure 1 shows a schematic of the tracing algorithm (we referenced implementation of `contour` function in MATLAB). For demonstration, a simple energy function $W(x, y) = \sqrt{x^2 + y^2}$ was assumed in the system (we dropped μ and K dependence), and a particle was initially located at $r_0 = 1.5$ and $\phi_0 = 20°$ (i.e., $x_0 \simeq 1.41$ and $y_0 \simeq 0.513$). Figure 1a shows the index space and values of W at grid nodes. The corresponding (x, y) coordinates are shown at the top and right axes. Each cell is labeled following the above definition. The steps of tracing are as follows: First, for the given initial location of the particle in Figure 1b, the initial cell location is found ($C_{4,3}$ in this case), and $W_0 = W(x_0, y_0)$ is linearly interpolated from the neighboring values at the cell vertices. In this simple example, one can immediately realize that $W_0 = 1.5$ is the initial radial distance of the particle location and that the trajectory (or contour line) should be circular and go through Edges 1 and 3 of $C_{4,3}$. Mathematically, if the contour line crosses Edge 1 of $C_{i,j}$, then the condition

$$(W_0 - W_{i,j}) \times (W_0 - W_{i+1,j}) < 0 \tag{4}$$

must be satisfied (conditions for other edges are straightforward). In our method, the search starts from Edge 1 through Edge 4. In Figure 1b, the search stops after Edge 1 has been
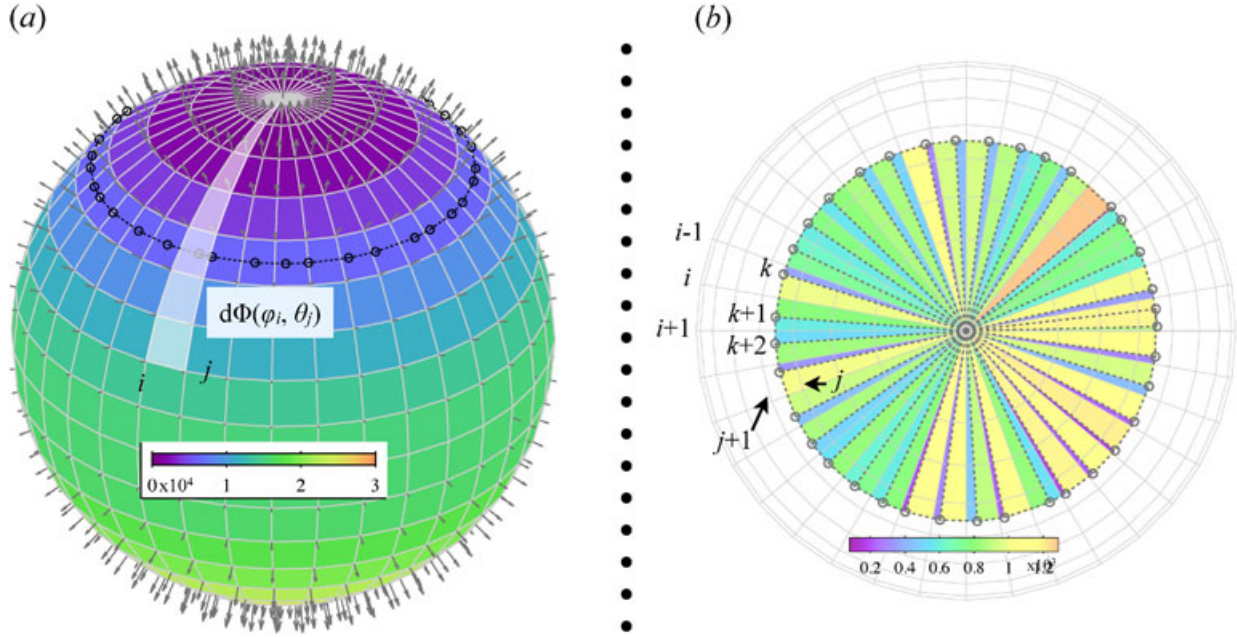
Figure 2. (a) Magnitude of the radial component of the magnetic field $|B_r|$ on the surface of the Earth is shown as arrows on the spherical grid. The magnitude of $d\Phi(\phi, \theta)$ is represented as the background color on the sphere. Open circles represent the footpoints of the drift orbit (an equatorially mirroring particle at approximately $2\ R_E$). (b) Projection of the grid space of the Northern Hemisphere in Figure 2a on the equator. The open circles represent the footpoints of the drift orbit. The dashed lines define the area through which the magnetic flux passes. The magnetic flux at each piece of wedge is represented with color scale. (i, j) index represents the spherical grid and k the footpoints.

tested because it is the first one that satisfies the condition. Once an edge is found, the coordinate of the intersection (asterisk symbol) determined using linear interpolation is recorded, and the algorithm moves to the neighboring cell that shares the edge that has been found ($C_{4,2}$; Figure 1c). Next, since one edge has already been found from the previous cell, there is only one edge to be found (Edge 1 of $C_{4,2}$). From this stage, the visited cells are also flagged. Last, this process continues until the contour line is closed (if the tracing algorithm comes back to the initial cell) or the boundary is encountered. Special care is needed when one of two terms in equation (4) becomes zero because where the contour line would go after passing a node is unpredictable (there are three cells that the contour can enter). In this implementation, we add an infinitesimal number to the term that results in zero so that equation (4) does not ever become zero.

[13] It is clear from the above example that not all W values would be used to trace a contour line and successive traces are most likely to use the W values that were used during the previous traces. In this implementation, we allocate a memory block for W but defer the evaluation until actual tracing. While tracing a contour line by the above procedure, the tracing algorithm checks for the existence of the W value at a node that the tracing module asked for. If not present, the algorithm dynamically evaluates and caches it before handing it over to the tracing module. Otherwise, it returns the cached W value. Overall, only those W values that are needed for tracing are evaluated at most once and reused as much as possible during the entire calculation. In this way, calls to the expensive evaluation of equation (1) are minimized.

2.4. Magnetic Flux Integration

[14] The scheme of magnetic flux integration in equation (3) is described next. For the integration, the drift orbit is mapped on the surface of the Earth. The footpoints of the orbit can be interpolated from the footpoints obtained on the nodes during the tracing. For numerical integration of equation (3), we discretize Earth's surface and calculate radial component of the magnetic field B_r (only this component is needed) at grid nodes, as shown in Figure 2a. The grid spacing is on the order of a degree in ϕ and less than a degree in θ coordinates where ϕ and θ are the usual spherical coordinates. We keep $\Delta\theta$ small because of the steep change in B_r with θ. Then equation (3) may be written as

$$\Phi = \oint \left[\int_0^{\theta(\phi)} |B_r| r^2 \sin\theta \, d\theta \right] d\phi = \oint d\Phi(\phi, \theta(\phi)). \quad (5)$$

Note that the absolute value of B_r is used. The integrand $d\Phi(\phi_i, \theta_j)$ represents the approximated magnetic flux through the area defined by the vertical white stripe in Figure 2a.

[15] At initialization, we calculate $d\Phi(\phi_i, \theta_j)$ using trapezoidal rule. This approach frees some computational overhead for evaluation of equation (5) because the last term in that equation is approximated by a one-dimensional summation

$$\Phi \simeq \sum_k d\Phi(\phi_k, \theta_k), \quad (6)$$

once $\theta(\phi)$ is given from the tracing. The index k denotes the kth footpoint of the closed drift orbit. Note that the magnetic flux of the Earth's magnetic field Φ_0 can be obtained
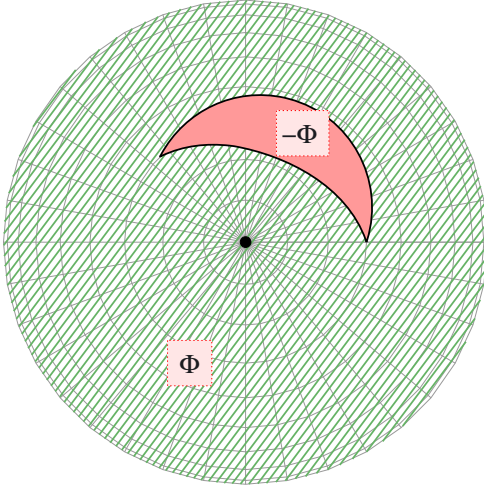
Figure 3. Schematic of the trapped drift orbit and its magnetic flux. The magnitude of the flux through the hatched area is equal to the magnitude of the flux through the shaded area.

from equation (5) using $\theta(\phi) = \pi$, i.e., $2\Phi_0 = -\oint d\Phi(\phi, \pi)$. We take this general approach to get Φ_0 because k_0 (Earth's magnetic moment) is not known in general. One needs to calculate $d\Phi$ only once whenever the magnetic field configuration changes.

[16] The footpoints of the drift orbit are irregularly spaced, and thus evaluation of equation (6) needs one more step. Figure 2b shows the grid space of the Northern Hemisphere projected onto the equator. Let us assume that one grid boundary at ϕ_i is located between the two footpoints, as in Figure 2b. In order to evaluate the magnetic flux through the stripe defined by (ϕ_k, θ_k) and $(\phi_{k+1}, \theta_{k+1})$ footpoints, the area should be separated at ϕ_i because the fluxes on both sides are not the same. Then the flux through the stripe is the sum of the fluxes through two stripes between ϕ_k and ϕ_i and between ϕ_i and ϕ_{k+1}. Taking into account the fact that θ_k is not on the integral grid, the flux can be approximated by interpolation as follows:

$$
\begin{aligned}
&d\Phi(\phi_{k+1}, \theta_{k+1}; \phi_k, \theta_k) \\
&= \left[d\Phi(\phi_i, \theta_j) + \Delta\theta_k(d\Phi(\phi_i, \theta_{j+1}) - d\Phi(\phi_i, \theta_j)) \right] \Delta\phi_k \\
&+ \left[d\Phi(\phi_{i+1}, \theta_j) + \Delta\theta_{k+1}(d\Phi(\phi_{i+1}, \theta_{j+1}) - d\Phi(\phi_{i+1}, \theta_j)) \right] \Delta\phi_{k+1},
\end{aligned}
\tag{7}
$$

where $\Delta\phi_k = \phi_{i+1} - \phi_k$, $\Delta\phi_{k+1} = \phi_{k+1} - \phi_{i+1}$, $\Delta\theta_k = (\Delta\phi_k(\theta_{k+1} - \theta_k)/(\phi_{k+1} - \phi_k) + \theta_k)/2$, and $\theta_{k+1} = (\Delta\phi_k(\theta_{k+1} - \theta_k)/(\phi_{k+1} - \phi_k) + \theta_{k+1})/2$. Generalization of the cases in which there are more than one ϕ boundary or none between two footpoints is straightforward. Finally, the total magnetic flux through the polar cap is evaluated using equations (6) and (7).

2.5. L^* in a Magnetic Island

[17] Storm time distortion of the magnetic field can cause a localized extremum in the total energy distribution (equation (2)), especially for high pitch angle particles, and transition of a particle in and out of this localized region can cause discontinuous jump with sign change in the magnetic flux [*Ukhorskiy et al.*, 2006]. Although this effect is not our main interest in this paper, for generality we describe how to deal with the drift orbit around the island. Figure 3 shows

the drift orbit of a trapped particle in the island mapped on the polar cap (solid curve, shown in the same format as Figure 2b). Integration of equation (3) is taken over the hatched area. From the divergence-free condition, the flux integrated over the hatched area has the same magnitude as the flux integrated within the area (shaded area in the figure) defined by the drift orbit and an opposite sign. If the drift orbit does not encircle the Earth, then $\oint d\phi = 0$. If it is the case, the resulting L^* will have negative sign.

3. Performance Analysis

[18] A performance analysis for the speed and accuracy of calculating L^* is presented in this section. While the formulation itself is applicable to a general equipotential field line assumption, a constant electric potential in all space (zero electric field) was assumed for the analysis, which is generally assumed for L^* calculation [e.g., *Roederer*, 1970].

3.1. Analytic Magnetic Field

[19] For validation, we use a compressed dipole field [*Elkington et al.*, 2003; *Kabin et al.*, 2007]

$$
\begin{aligned}
\mathbf{B} &= \mathbf{e}_r \left(\frac{2k_0}{r^3} - b_1(1 + b_2 \cos\phi) \right) \cos\theta \\
&+ \mathbf{e}_\theta \left(\frac{k_0}{r^3} + b_1(1 + b_2 \cos\phi) \right) \sin\theta, \\
\mathbf{A} &= \mathbf{e}_\phi \left(\frac{k_0}{r^2} - \frac{r}{2} b_1(1 + b_2 \cos\phi) \right),
\end{aligned}
\tag{8}
$$

where k_0 is the Earth's magnetic moment, and parameters b_1 and b_2 describe the distortion of the dipole field: b_1 can be interpreted as a quantity related to the interplanetary magnetic field strength, and b_2 is a nondimensional parameter responsible for the azimuthal asymmetry of the resulting field (influenced, to a large degree, by the solar wind dynamic pressure). When $b_1 = 0$, the magnetic field becomes a symmetric dipole field, and L^* reduces to the dipole L value. Despite the simple analytic form, equation (3) may not be solved analytically if $b_1 \neq 0$. One special case is when the pitch angle is 90°. Then the drift path is analytically given from the initial location (r_0, ϕ_0) by

$$
r(\phi; r_0, \phi_0) = r_0 \sqrt[3]{\frac{k_0}{k_0 - b_1 b_2 r_0^3 (\cos\phi_0 - \cos\phi)}}.
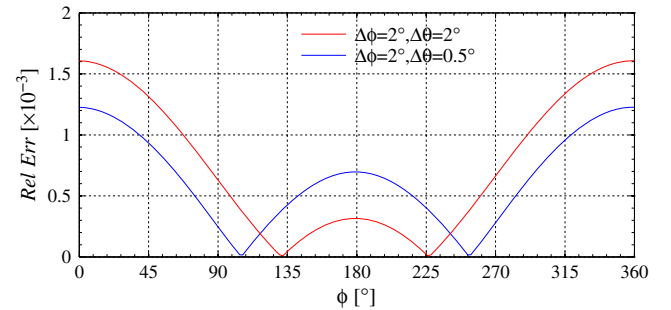\tag{9}
$$

Figure 4. Relative error of the numerically evaluated magnetic flux to the analytic solution using the asymmetric magnetic field. $\Delta\theta$ is set to 2° (red), and 0.5° (blue), and $\Delta\phi$ is fixed to 2°.
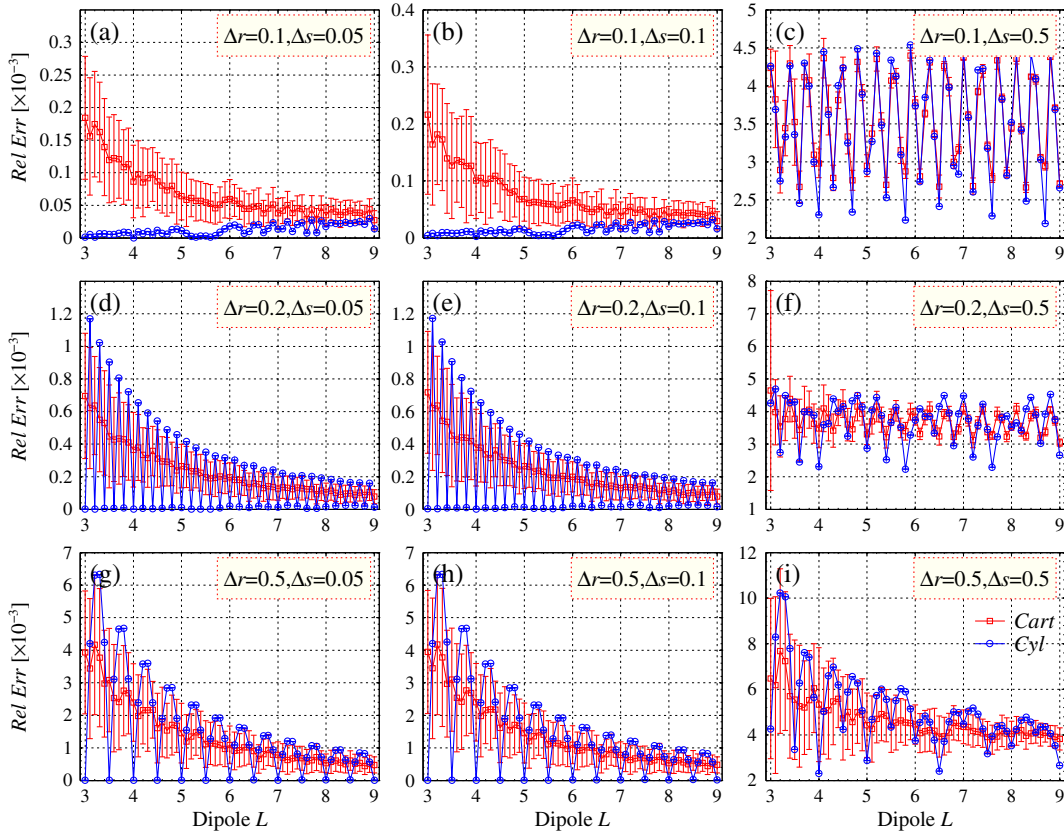
Figure 5. Relative error of L^* computed in the dipole field using both rectangular (red) and cylindrical (blue) grids as a function of dipole L. Δr and Δs increase toward the bottom and right panels, respectively. That is, panels (a), (b) and (c) represent results for Δs = 0.05, 0.1, and 0.5 R_E, and panels (a), (d), and (g) represent results for Δr = 0.1, 0.2, and 0.5 R_E, respectively.

The magnetic flux, Φ can then be numerically evaluated as accurate as the machine precision using the first form of equation (3).

[20] In the following analysis, we use both the dipole field for all pitch angles and the asymmetric magnetic field with parameters b_1 = 5 nT and b_2 = 4 (referred to as the asymmetric magnetic field hereafter) for 90° pitch angle. k_0 is set to 31,200 nT R_E^3.

3.2. Accuracy of Magnetic Flux Integration

[21] The accuracy of the numerical evaluation of the magnetic flux integration was estimated using the asymmetric magnetic field. $d\Phi(\phi, \theta)$ in equation (5) with the asymmetric magnetic field (equation (8)) is $d\Phi_{\text{analytic}}(\phi, \theta) = \frac{1}{2}\sin^2\theta(2k_0 - b_1(1 + b_2\cos\phi))d\phi$. Shown in Figure 4 is the relative error of the numerically calculated magnetic flux, $Rel\,Err(\phi_i, \theta_j) = \langle|\Delta\Phi_{\text{cal},ij} - \Delta\Phi_{\text{analytic},ij}|/\Delta\Phi_{\text{analytic},ij}\rangle_j$. Notation $\langle\rangle_j$ denotes the averaging operation along j index. The result shows that, when the resolution of θ coordinate is on the order of 1°, the numerical error is on the order of 10^{-3}, and the error only weakly depends on the resolution of ϕ coordinate (not shown) because the magnitude of the magnetic field on the Earth's surface is nearly azimuthally symmetric.

3.3. Accuracy of L^*

[22] We analyzed the relative error of the calculated L^* to the exact L^* with the dipole field and asymmetric

magnetic field. We also sought the appropriate grid resolution which balances accuracy and computational cost. Both cartesian and cylindrical grids were used for comparison. Spatial resolution $(\Delta r, \Delta\phi)$ and field line integration step size (Δs, corresponding to the resolution in K space) were set as follows: Δr = (0.1, 0.2, 0.5) R_E, $\Delta\phi$ = (1, 2, 5)°, and Δs = (0.05, 0.1, 0.5) R_E. For the rectangular grid, $\Delta x = \Delta y = \Delta r$. As discussed earlier, the resolution in $\Delta\phi$ is not a major source of inaccuracy of the magnetic flux integration. Shown below are only the cases where $\Delta\phi$ = 2°. $\Delta\theta$ was set to 0.25°.

[23] Figure 5 shows the relative error of the calculated L^* values in the dipole field model. Δr and Δs increase in moving toward the bottom and the right, respectively. Initial locations were regularly spaced from 3 to 9 R_E separated by 0.1 R_E in radial distance (r_0) and from 10° to 90° separated by 1° in pitch angle (α_0). The azimuthal angles (ϕ_0) were randomly chosen in order to avoid the bias at grid nodes. The relative error is defined as $Rel\,Err(r_0) = \langle|L^*_{\text{cal}}(r_0, \alpha_0) - L^*_{\text{exact}}(r_0, \alpha_0)|/L^*_{\text{exact}}(r_0, \alpha_0)\rangle_{\alpha_0}$, and one standard deviation is also calculated in a similar manner. We note a few key features of these results: first, the relative errors, especially in the first two columns, in the rectangular grid show a decreasing trend as L^* increases. If the absolute errors were shown, dependence of the error on L^* would be minimized. Second, due to the cylindrical symmetry of the dipole field, L^* values calculated at the radial grid boundary in the cylindrical grid are very accurate (order of 10^{-5})
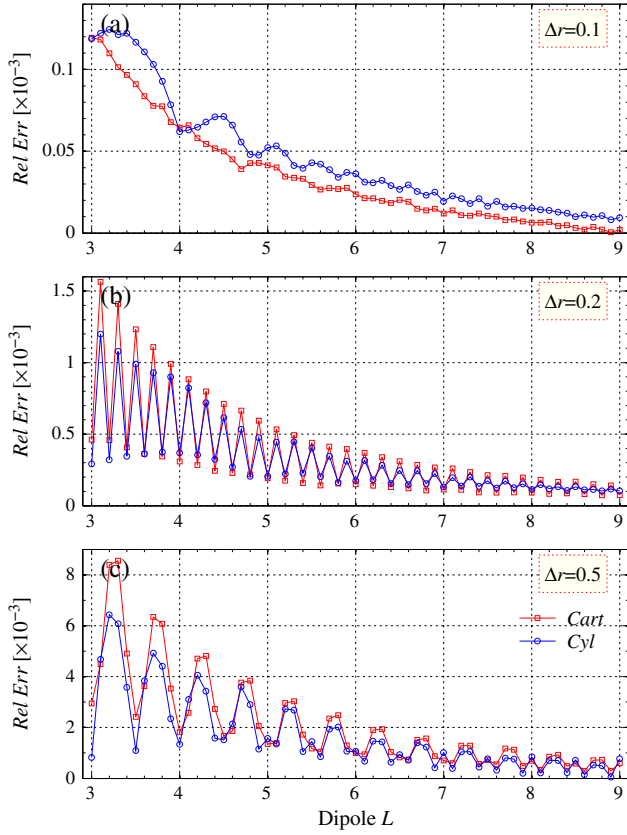
Figure 6. Relative error of L^* computed in the asymmetric magnetic field using both rectangular (red) and cylindrical (blue) grids as a function of dipole L. Δr increases toward the bottom panel, and Δs is set to 0.1 R_E.

as in Figures 5a and 5b. On the other hand, the error at the non-integral grid is comparable to that of the rectangular grid, as in Figures 5d and 5e (note peaks between the radial grid boundaries). This caused the oscillatory behavior in the relative error for $\Delta r \geq 0.2$. We tried weighted interpolation based on the dipole geometry but did not show significant improvement. The oscillatory behavior for the rectangular grid is less prominent because of the pitch angle dependence of the calculated L^* (as will be discussed shortly) and the random choice of the initial azimuthal coordinates (the cylindrical grid will not be affected by the azimuthal coordinates in the dipole field). Third, the standard deviation in the rectangular grid is noticeable compared to that in the cylindrical grid (essentially zero). Although not heavily investigated, we suspect that the areal interpolation of the field line quantities may cause the pitch angle dependence. On the other hand, the areal interpolation in the cylindrical grid essentially becomes 1-D linear interpolation in the azimuthal direction on which the dipole field has symmetry. Last, we also used finer grid spacing, but there was no significant improvement in accuracy (not shown), which may indicate an inherent upper limit ($\sim 10^{-5}$) of the achievable accuracy.

[24] Figure 6 shows the relative error of the calculated L^* values in the asymmetric magnetic field. Δr increases moving down the panels. The initial locations were distributed in radial distance from 3 to 9 R_E separated by 0.1 R_E. ϕ_0 and θ_0

coordinates were set to 0° (noon) and 90°, respectively. Note that Δs is fixed to 0.1 R_E because the dependence on Δs is meaningless for the equatorial particles. The result indicates that the relative error behaves as expected for the symmetric case. Due to the asymmetry, the errors for both grids behave similarly, and thus the absolute errors would be less dependent on the L^* as well. The oscillatory behavior in the relative error for the coarser grids is also clear due to the same reason as the previous result. The clear oscillation for the rectangular grid is because the particles were traced from the same local time (noon meridian).

3.4. Calculation Speed

[25] The calculation speed is estimated next for several Tsyganenko magnetic field models [*Tsyganenko*, 1987, 1989, 1995; *Tsyganenko and Sitnov*, 2005, 2007; *Sitnov et al.*, 2008] with the dipole field as control. Since the dipole field is simplest, the algorithm is the major contributing factor to the calculation speed in this field. In other words, the calculation speed in the dipole field forms the baseline, and the speed above this line is solely due to the model field. A standard laptop with 2.8 GHz Intel Core 2 Duo processor was used for all the tests. The calculation speed is defined as total elapsed time per particle and core. $\Delta s = 0.1\,R_E$ and $\Delta r = 0.2\,R_E$ were used for the grid resolutions (which we think is a reasonable choice for accuracy versus speed). Figure 7 shows the speed as a function of model. The tests were done using 2 day Van Allen Probe orbit (Figure 8). In the dipole field, the speed is about 6 ms, which is the baseline. For the T96 model, it takes about half a second, and for the T02 and TS05 models about a second. For the TS07 model, it takes an order of magnitude longer than the TS05 model. Based on this result, the new L^* calculation method may be faster than any other physics-based methods currently available.

4. Scientific Application: L^* Coordinate of Satellite Orbit

[26] Two major uses of the L^* coordinate are (1) real-time satellite tracking in the L^* coordinate and (2) mapping between invariant space and phase space. The application of the former is shown in this section, and that of the latter is briefly discussed in the next section. For the purpose
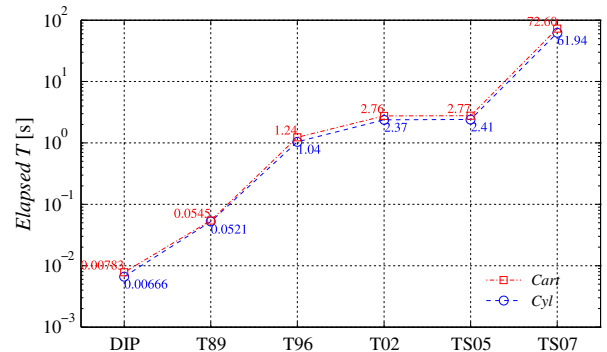

Figure 7. Calculation speed of a single trajectory as a function of model for rectangular (square symbol) and cylindrical (open circle) grids. The exact speed at the symbols is labeled within the plot.
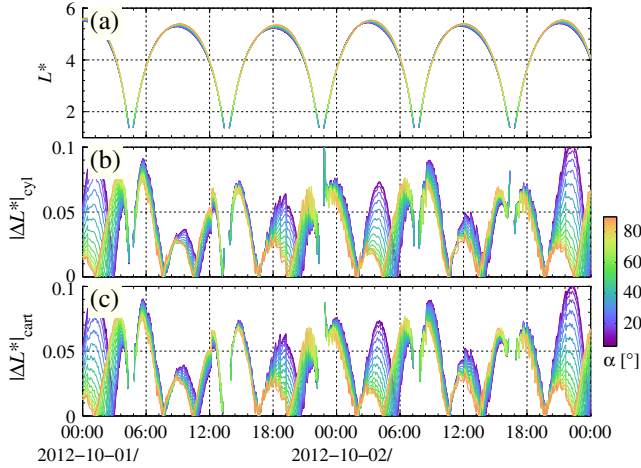
Figure 8. (a) Calculated L^* coordinates of the spacecraft orbit using the cylindrical grid as a function of time and pitch angle. (b) The magnitude of the difference between two methods with the cylindrical grid. (c) The magnitude of the difference between two methods with the rectangular grid.

of demonstrating the capability of a real-time computation, we calculate the L^* coordinate of the 2 day long Van Allen Probe-A orbit. For the performance benchmark, we compare our calculated L^* values to those of LANLGeoMag. LANL-GeoMag uses the T89Q field model (T89 field model with Kp = 2) among other various field models. In this test, T89Q model was used (for other models, model parameters were not explicitly given). $\Delta s = 0.1\,R_E$ and $\Delta r = 0.2\,R_E$ are used for the grid resolution in our method.

[27] Figure 8a shows the calculated L^* coordinates, and Figures 8b and 8c show the magnitude of L^* difference between two methods for the cylindrical and rectangular grids, respectively. The deviation is about 0.1 at maximum (around $L^* \sim 3$) and is largest at lower pitch angles for both coordinate systems. It took about 1350 and 1413 s for the cylindrical and rectangular grids, respectively, to produce the results.

5. Discussion

5.1. A Comparison Between Our New Method and the Technique of *Roederer* [1970]

[28] Even though the development of the method was motivated by (U, B, K) coordinates [*Whipple*, 1978], we realized that this method is essentially an extension of the technique of *Roederer* [1970]. Both methods are based on the same underlying physics and assumptions. One major difference is from the drift orbit tracing. Figure 9 demonstrates the tracing technique of *Roederer* [1970], stating that the field lines that have the same initial invariants and the magnitude of the magnetic field at mirror points are iteratively searched by more or less arbitrarily probing adjacent field lines separated by a small distance (step size). The advantage of our tracing algorithm is that a fully closed drift orbit is always guaranteed to be found regardless of the grid resolution. This is somewhat difficult in the technique of *Roederer* [1970] because of error accumulation at each iteration.

5.2. Mapping Between L^* and x-y Coordinates

[29] In diffusion simulation, it is often required to convert phase space density in invariant space to differential flux in phase space for comparison with observations. In this section, the performance gain of our technique is further demonstrated when calculating the mapping between L^* and x-y coordinates with a complex magnetic field model.

[30] When the number of calculations become large, the speed ultimately scales solely by the complexity of the model field. In practice, the magnetic fields are often approximated from the tabulated field vectors in a cubic grid space (e.g., field interpolation in MHD simulation). Due to the dimensionality, pre-allocating a chunk of memory block and precalculating the vector field in advance may be too costly. As shown in section 2.3, most of the magnetic fields at grid nodes would not be consumed. By taking the similar approach for the drift shell tracing, we show the speed and accuracy, without describing the implementation.

[31] Figure 10a shows the error as a function of spatial location. The error is defined as the averaged magnitude (in pitch angle) of difference of the calculated L^* values between the analytic field and interpolated field. Since the purpose of this test is to examine the deviation resulted from using the interpolated field, the accuracy of L^* values of the control is not an issue here as long as the same tracing program is used. The asymmetric magnetic field was used for the analytic field. $\Delta x = \Delta y = \Delta z = 0.1\,R_E$ was used for the cubic grid resolution, and initial locations were evenly distributed from 2 to $9\,R_E$ separated by $0.2\,R_E$ in radial direction and from $0°$ to $360°$ separated by $4°$ in azimuthal direction. Pitch angles from $10°$ to $90°$ were evenly divided into 17 bins. The order of error is 10^{-3}, and the large error occurs at the tail where the field lines are stretched.

[32] Figure 10b shows the mapping from x-y coordinates to L^* values under the latest TS07 field model using parameters during the prestorm period (for model parameters, http://geomag_field.jhuapl.edu/model/). Initial locations were the
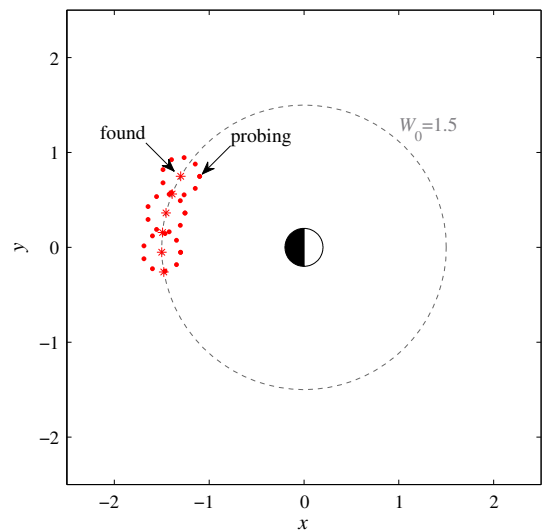

Figure 9. Schematic showing the technique of *Roederer* [1970]. Dots are probing points, and asterisks are approximated equatorial intersection of the shell field lines. Figure format is similar to Figure 1.
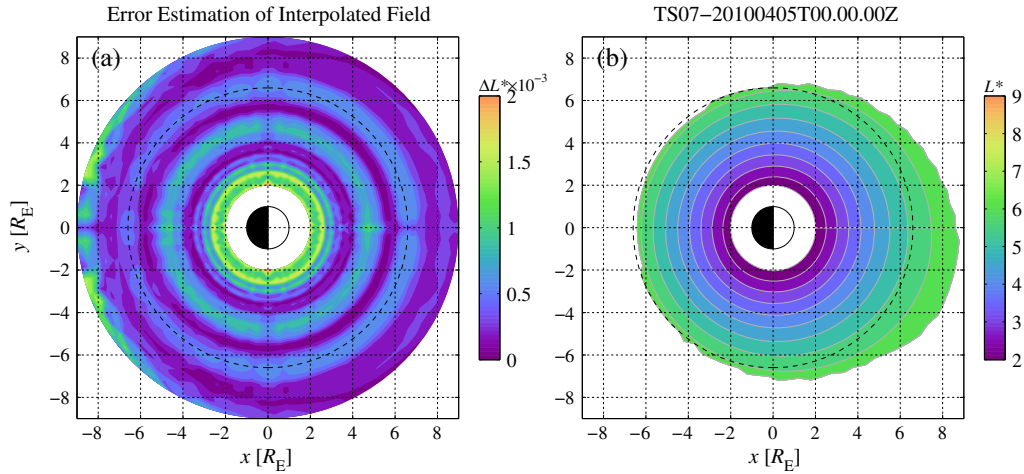
Figure 10. (a) Absolute error in calculated L^* using the interpolated field. Undefined L^* values (due to losses through the magnetopause and ionosphere) were excluded from the average. (b) Calculated L^* of 88° pitch angle using the interpolated TS07 field model as a function of x-y coordinates. The dashed circles are at 6.6 R_E.

same as before. The result of 90° (88° to be precise) pitch angle particles is only shown. The 90° pitch angle particles often fail the bifurcation test due to the scratchy field line from the interpolation. The elapsed time was 1312 s when both CPU cores were fully loaded. According to the result in Figure 7, it would have taken 19 days to produce the result. The calculation speed demonstrates the significant performance gain of our technique described in section 2.3, especially for a complex magnetic field model. Such a scalability is an added advantage of our method and enables us to calculate a large number of L^* values as often required for intercomparison between the simulation result and the observation.

6. Summary

[33] The algorithm and implementation of a new, efficient method for calculating L^* have been thoroughly described. While this method may be regarded as an extension of the technique of *Roederer* [1970], it has a major difference from the latter technique in that our technique of tracing in a finite grid is free from error accumulation and ensures the existence of a closed drift orbit. The main improvement over the method described in Paper 1 results from eliminating the "preparation step" in which the functional relationship between K and B_m is calculated in advance. Realizing that not all W values are needed for tracing a drift trajectory, the new method instead evaluates $K(B_\mathrm{m})$ only at necessary grid points at the time of tracing.

[34] From the results of performance analyses, we believe that the new method is able to calculate L^* values faster than any other physics-based methods currently available. The method can transform the satellite orbit from configuration space to L^* space in near real time and is highly scalable to a large number of L^* values with reducing incremental cost. Despite a possible inherent limit due to the use of a finite grid, we suggest that this method could be an added resource for the radiation belt community.

References

Boscher, D., S. Bourdarie, P. O'Brien, and T. Guild (2012). IRBEM-LIB library, http://irbem.sourceforge.net (last accessed: 10th June 2012).

Cary, J. R., and A. J. Brizard (2009), Hamiltonian theory of guiding-center motion, *Rev. Mod. Phys.*, *81*(2), 693–738, doi:10.1103/RevModPhys.81.693.

Elkington, S. R., M. K. Hudson, and A. A. Chan (2003), Resonant acceleration and diffusion of outer zone electrons in an asymmetric geomagnetic field, *J. Geophys. Res.*, *108*(A3), 1116, doi:10.1029/2001JA009202.

Kabin, K., R. Rankin, A. W. Degeling, and R. Marchand (2007), Polarization properties of field line resonances in non-axisymmetric background magnetic fields, *Ann. Geophys*, *25*(3), 815–822, doi:10.5194/angeo-25-815-2007.

Koller, J., and S. Zaharia (2011), LANL* V2.0: Global modeling and validation, *Geosci. Model Dev.*, *4*, 669–675, doi:10.5194/gmd-4-669-2011.

Koller, J., G. D. Reeves, and R. H. W. Friedel (2009), LANL* V1.0: A radiation belt drift shell model suitable for real-time and reanalysis applications, *Geosci. Model Dev.*, *2*, 113–122, doi:10.5194/gmd-2-113-2009.

Mauk, B. H., N. J. Fox, S. G. Kanekal, R. L. Kessel, D. G. Sibeck, and A. Ukhorskiy (2012), Science objectives and rationale for the Radiation Belt Storm Probes Mission, *Space Sci. Rev.*, 1–15, doi:10.1007/s11214-012-9908-y.

McCollough, J. P., J. L. Gannon, D. N. Baker, and M. Gehmeyr (2008), A statistical comparison of commonly used external magnetic field models, *Space Weather*, *6*, S10001, doi:10.1029/2008SW000391.

Min, K., J. Bortnik, and J. Lee (2013), A novel technique for rapid L^* calculation using UBK coordinates, *J. Geophys. Res.*, *118*, 1–6, doi:10.1029/2012JA018177.

Northrop, T. G., and E. Teller (1960), Stability of the adiabatic motion of charged particles in the Earth's field, *Phys. Rev.*, *117*(1), 215–225, doi:10.1103/PhysRev.117.215.

Roederer, J. G. (1970), *Dynamics of Geomagnetically Trapped Radiation*, pp. 84–106, Springer, New York.

Schulz, M., and L. J. Lanzerotti (1974), *Particle Diffusion in the Radiation Belts*, vol. 7, pp. 10–39, Springer, Berlin.

Sheldon, R. B., and J. D. Gaffey (1993), Particle tracing in the magnetosphere: New algorithms and results, *Geophys. Res. Lett.*, *20*(9), 767–770, doi:10.1029/93GL00835.

Sitnov, M. I., N. A. Tsyganenko, A. Y. Ukhorskiy, and P. C. Brandt (2008), Dynamical data-based modeling of the storm-time geomagnetic field with enhanced spatial resolution, *J. Geophys. Res.*, *113*, A07218, doi: 10.1029/2007JA013003.

Tsyganenko, N. A. (1987), Global quantitative models of the geomagnetic field in the cislunar magnetosphere for different disturbance levels, *Planet. Space Sci.*, *35*, 1347–1358, doi:10.1016/0032-0633(87)90046-8.

Tsyganenko, N. A. (1989), A magnetospheric magnetic field model with a warped tail current sheet, *Planet. Space Sci.*, *37*, 5–20, doi: 10.1016/0032-0633(89)90066-4.

Tsyganenko, N. A. (1995), Modeling the Earth's magnetospheric magnetic field confined within a realistic magnetopause, *J. Geophys. Res.*, *100*(A4), 5599–5612, doi:10.1029/94JA03193.

Tsyganenko, N. A. (2002a), A model of the near magnetosphere with a dawn-dusk asymmetry: 1. Mathematical structure, *J. Geophys. Res.*, *107*(A8), 1179, doi:10.1029/2001JA000219.

Tsyganenko, N. A. (2002b), A model of the near magnetosphere with a dawn-dusk asymmetry: 2. Parameterization and fitting to observations, *J. Geophys. Res.*, *107*(A8), 1176, doi:10.1029/2001JA000220.

Tsyganenko, N. A., and M. I. Sitnov (2005), Modeling the dynamics of the inner magnetosphere during strong geomagnetic storms, *J. Geophys. Res.*, *110*, A03208, doi:10.1029/2004JA010798.

Tsyganenko, N. A., and M. I. Sitnov (2007), Magnetospheric configurations from a high-resolution data-based magnetic field model, *J. Geophys. Res.*, *112*, A06225, doi:10.1029/2007JA012260.

Ukhorskiy, A. Y., B. J. Anderson, P. C. Brandt, and N. A. Tsyganenko (2006), Storm time evolution of the outer radiation belt: Transport and losses, *J. Geophys. Res.*, *111*, A11S03, doi:10.1029/2006JA011690.

Whipple, E. C. (1978), (U, B , K) coordinates: A natural system for studying magnetospheric convection, *J. Geophys. Res.*, *83*(A9), 4318–4326, doi: 10.1029/JA083iA09p04318.

Yu, Y., J. Koller, S. Zaharia, and V. Jordanova (2012), L^* neural networks from different magnetic field models and their applicability, *Space Weather*, *10*, S02014, doi:10.1029/2011SW000743.